J. Fluid Mech. (2022), *vol.* 932, A23, doi:10.1017/jfm.2021.1012

Kinetic-energy-flux-constrained model using an artificial neural network for large-eddy simulation of compressible wall-bounded turbulence

Changping Yu[1,2], Zelong Yuan[3], Han Qi[1,2], Jianchun Wang[3,]†, Xinliang Li[1,2,]† and Shiyi Chen[3,4]

[1]LHD, Institute of Mechanics, Chinese Academy of Sciences, Beijing 100190, PR China

[2]School of Engineering Science, University of Chinese Academy of Sciences, Beijing 100049, PR China

[3]Department of Mechanics and Aerospace Engineering, Southern University of Science and Technology, Shenzhen 518055, PR China

[4]State Key Laboratory of Turbulence and Complex Systems, College of Engineering, Peking University, Beijing 100871, PR China

(Received 2 June 2021; revised 3 November 2021; accepted 9 November 2021)

Kinetic energy flux (KEF) is an important physical quantity that characterizes cascades of kinetic energy in turbulent flows. In large-eddy simulation (LES), it is crucial for the subgrid-scale (SGS) model to accurately predict the KEF in turbulence. In this paper, we propose a new eddy-viscosity SGS model constrained by the properly modelled KEF for LES of compressible wall-bounded turbulence. The new methodology has the advantages of both accurate prediction of the KEF and strong numerical stability in LES. We can obtain an approximate KEF by the tensor-diffusivity model, which has a high correlation with the real value. Then, using the artificial neural network method, the local ratios between the real KEF and the approximate KEF are accurately modelled. Consequently, the SGS model can be improved by the product of that ratio and the approximate KEF. In LES of compressible turbulent channel flow, the new model can accurately predict mean velocity profile, turbulence intensities, Reynolds stress, temperature–velocity correlation, etc. Additionally, for the case of a compressible flat-plate boundary layer, the new model can accurately predict some key quantities, including the onset of transitions and transition peaks, the skin-friction coefficient, the mean velocity in the turbulence region, etc., and it can also predict the energy backscatters in turbulence. Furthermore, the proposed model also shows more advantages for coarser grids.

Key words: compressible turbulence, turbulence modelling

---

† Email addresses for correspondence: wangjc@sustech.edu.cn, lixl@imech.ac.cn

1. Introduction

Large-eddy simulation (LES) has achieved great success in the numerical investigation of turbulent flows, and it has already been widely used in studying the mechanism of turbulence and in simulating practical engineering flows (Larchevêque *et al.* 2004; Fureby 2008). The most widely used subgrid-scale (SGS) model is the eddy-viscosity model (Lesieur & Métais 1996), and the first SGS eddy-viscosity model was the Smagorinsky model (Smagorinsky 1963; Deardorff 1970). Using the eddy-damped quasi-normal Markovian theory, Chollet & Lesieur (1981) suggested the spectral eddy-viscosity model, which is suitable for homogeneous and isotropic turbulence. Based on the square of the velocity gradient tensor, Nicoud & Ducros (1999) proposed a wall-adapting local eddy-viscosity model (WALE), which can well simulate wall-bounded flows without a dynamic procedure. The Vreman (2004) model is another SGS eddy-viscosity model suitable for the LES of turbulent shear flows. Yu *et al.* (2013) presented a new form of SGS viscosity according to SGS helicity dissipation balance and a spectral relative helicity relation in the inertial subrange of helical turbulence, and this model can simulate shear and separated turbulent flows with satisfactory results. Recently, Pickering *et al.* (2021) proposed a data-informed method to test which eddy-viscosity model could improve the alignment between observed large-scale structures and those computed from resolvent analysis. Leoni *et al.* (2021) developed a new eddy-viscosity model based on fractional gradients, and it could accurately predict the non-local behaviour of subfilter stress–strain-rate correlation functions. In addition to the eddy-viscosity model, the structural model is an important type of SGS model, which provides a high correlation with the real SGS stress (Meneveau & Katz 2000). One of the structural models is the gradient model, which was originally proposed by Clark, Ferziger & Reynolds (1979) and then was developed by Vreman, Geurts & Kuerten (1996). The gradient model can be derived from the Taylor expansion of the filtered velocity for the SGS stress. The scale-similarity model (SSM) is another structural model, which is based on the scale-similarity hypothesis (Bardina, Ferziger & Reynolds 1980; Liu, Meneveau & Katz 1994). According to the assumption of scale invariance, the SSM is developed in a similar form as an SGS stress tensor of a larger-scale flow field using the resolved velocity, and the SSM also has a high correlation with the real SGS stress.

The famous dynamic procedure was proposed by Germano *et al.* (1991), using the Germano identity to dynamically determine the coefficient of the SGS model in the LES of turbulent flows. Subsequently, Lilly (1992), Piomelli (1993), Ghosal *et al.* (1995) and Meneveau, Lund & Cabot (1996) improved and generalized the dynamic procedure. With the Germano identity, Yu, Xiao & Li (2016) derived an expression for the energy flux at the test-filter scale, which can be adopted to optimize the coefficients of SGS models. Incorporating physical constraints into the SGS model can also improve the reliability and accuracy of the model. Chen *et al.* (2012) introduced Reynolds stress to constrain the SGS model in the inner layer of wall-bounded turbulent flows to make the prediction of mean velocity, turbulent stress and skin-friction coefficient more accurate, which is called the Reynolds-stress-constrained LES.

Nevertheless, the traditional LES requires further improvements in transitional flows (Sayadi & Moin 2012), compressible flows (Piomelli 1999) and low-Reynolds-number regions (Voke 1996; Meneveau & Katz 2000). Horiuti (1986) employed the standard Smagorinsky model (SM) to simulate the transitional channel flow and found that this model cannot properly predict the transition process due to excessive dissipation. Huai, Joslin & Piomelli (1997) applied the dynamic Smagorinsky model (DSM) to the simulation of a transitional flat-plate boundary layer for the first time and obtained acceptable results. Sayadi & Moin (2012) evaluated several commonly used SGS models in LES of transitional flows. They found that the dynamic procedure could accurately predict the transition. Recently, Bodart & Larsson (2012) proposed a laminar/turbulent sensor to the traditional wall model and successfully predicted the transition. Moin *et al.* (1991) suggested a compressible DSM model for the first time and applied the model to the simulation of compressible isotropic turbulence. Chai & Mahesh (2012) proposed a dynamic one-equation eddy-viscosity model for the LES of compressible flow and applied it to decaying isotropic turbulence and normal shock–isotropic turbulence interactions.

For the traditional LES, most SGS models are developed based on the scale-invariance hypothesis. Voke (1996) provided a fitted relation between the SGS viscosity of the SM and the mesh Reynolds number based on some theoretical models of the energy spectrum. This scale-dependent SM was an attempt to overcome the limitation of the scale-invariance hypothesis, and the simulation results were improved slightly when the cutoff was in the dissipation range. Meneveau & Lund (1997) proposed a fitting ratio of the test-scale to the grid-scale coefficient of the SM and applied the scale-dependent DSM to simulate forced isotropic turbulence. Porté-Agel, Meneveau & Parlange (2000) generalized the scale-dependent DSM to simulate a neutral atmospheric boundary layer.

More recently, artificial neural networks (ANNs) have become an increasingly popular method for developing turbulence models (Duraisamy, Iaccarino & Xiao 2019). Ling, Kurzawski & Templeton (2016) adopted a new multiplicative-layer neural network with an invariant tensor to predict the Reynolds stress anisotropic tensor for the first time. Taking advantage of machine learning and optimal evaluation theory, Vollant, Balarac & Corre (2017) developed a new SGS scalar flux model. The deconvolution of turbulence variables can also be obtained through an ANN (Maulik & San 2017), and it showed excellent behaviour in an *a priori* test. Zhou *et al.* (2019*b*) developed a new SGS model through the ANN method for isotropic turbulence, and it considered the dependence of the SGS model on the filter width. Xie *et al.* (2019) proposed an ANN-based mixed model combining the SM and the gradient model, and the new model showed better behaviour in *a priori* and *a posteriori* tests than traditional LES models. Using neural networks trained by full turbulent channel flow data, Yang *et al.* (2019) discussed several problems encountered in wall modelling of LES. Using the direct numerical simulation (DNS) data of incompressible isotropic turbulence, ANN-based nonlinear algebraic models and deconvolutional models have been developed (Xie, Wang & Weinan 2020*a*; Xie, Yuan & Wang 2020*b*; Yuan, Xie & Wang 2020), which could clearly improve the accuracy of the model compared with the traditional SGS models and implicit large-eddy simulation (ILES).

In addition, machine learning methods have been employed for super-resolution reconstruction of turbulent flows (Maulik & San 2017; Fukami, Fukagata & Taira 2019; Kim & Lee 2020; Liu *et al.* 2020; Yuan *et al.* 2020; Kim *et al.* 2021). Such reconstruction can be used to improve predictions based on coarse wall measurements in wall-bounded turbulence (Güemes *et al.* 2021; Vinuesa & Brunton 2021). In past studies, some completely black-box models based on ANN methods have been developed in LES modelling of wall-bounded turbulence. Through *a priori* test and *a posteriori* test, Park & Choi (2021) found that the SGS model is unstable with the input variables at multiple points, but stable with the input variables at a single point, and the single-point input variables will also be adopted in this study.

In this paper, we propose a kinetic-energy-, ux-constrained model (KCM) using the ANN method for the LES of compressible wall-bounded turbulence. The structure of the paper is as follows. The LES governing equations and modelling background are introduced in § 2. The theoretical deduction of the new constrained model is given in § 3, followed by the DNS of the compressible channel flow and the ANN method in § 4. In § 5, the LES results of compressible turbulent channel flow and the compressible flat-plate boundary layer are presented and analysed. Finally, the discussion and conclusions are given in § 6.

2. Theoretical background

2.1. *LES governing equations*

For the general applicability of the research, we derive the LES governing equations of compressible flows as follows:

$$\frac{\partial \bar{\rho}}{\partial t} + \frac{\partial \bar{\rho}\tilde{u}_j}{\partial x_j} = 0, \tag{2.1}$$

$$\frac{\partial \bar{\rho}\tilde{u}_i}{\partial t} + \frac{\partial \bar{\rho}\tilde{u}_i\tilde{u}_j}{\partial x_j} + \frac{\partial \bar{p}}{\partial x_i} = \frac{\partial \tilde{\sigma}_{ij}}{\partial x_j} - \frac{\partial \tau_{ij}}{\partial x_j}, \tag{2.2}$$

$$\frac{\partial \bar{\rho}\tilde{E}}{\partial t} + \frac{\partial (\bar{\rho}\tilde{E} + \bar{p})\tilde{u}_j}{\partial x_j} = -\frac{\partial \tilde{q}_j}{\partial x_j} + \frac{\partial \tilde{\sigma}_{ij}\tilde{u}_i}{\partial x_j} - \frac{\partial C_p Q_j}{\partial x_j} - \frac{\partial \mathcal{J}_j}{\partial x_j}, \tag{2.3}$$

$$\bar{p} = \bar{\rho} R \tilde{T}, \tag{2.4}$$

where an overbar $(\bar{\cdot})$ denotes spatial filtering at scale $\varDelta$ using a smooth low-pass filter function $G(\boldsymbol{r})$ (e.g. $\bar{\rho}(x) = \int G(\boldsymbol{r})\rho(x + r)\,\mathrm{d}\boldsymbol{r}$ represents the resolved density field) and a tilde $(\tilde{\cdot})$ denotes spatial Favre filtering as $\tilde{\phi} = \overline{\rho\phi}/\bar{\rho}$.

In (2.1)–(2.4), ρ, u_i, T, E and R denote the density, velocity, temperature, total energy and specific gas constant, respectively. The resolved viscous stress tensor $\tilde{\sigma}_{ij}$ and the heat flux vector $\tilde{q}_j$ are given by

$$\tilde{\sigma}_{ij} = 2\mu(\tilde{T})(\tilde{S}_{ij} - \tfrac{1}{3}\delta_{ij}\tilde{S}_{kk}), \tag{2.5}$$

$$\tilde{q}_j = \frac{C_p \mu(\tilde{T})}{Pr}\frac{\partial \tilde{T}}{\partial x_j}, \tag{2.6}$$

where C_p and Pr are the specific heat at constant pressure and the molecular Prandtl number, $\mu = (1/Re)(\tilde{T}/\tilde{T}_\infty)^{3/2}[(\tilde{T}_\infty + T_s)/(\tilde{T} + T_s)]$ is the molecular viscosity calculated using Sutherland's law for a given $T_s = 110.3$ K, $Re = \rho_\infty U_\infty L/\mu_\infty$ is the Reynolds number and $\tilde{S}_{ij} = \frac{1}{2}(\partial \tilde{u}_i/\partial x_j + \partial \tilde{u}_j/\partial x_i)$ is the resolved strain-rate tensor.

In (2.1)–(2.3), there are some unclosed terms, including the SGS stress tensor

$$\tau_{ij} = \bar{\rho}(\widetilde{u_i u_j} - \tilde{u}_i\tilde{u}_j), \tag{2.7}$$

the SGS heat flux

$$Q_j = \bar{\rho}(\widetilde{u_j T} - \tilde{u}_j\tilde{T}) \tag{2.8}$$

and the SGS turbulent diffusion

$$\mathcal{J}_j = \tfrac{1}{2}(\bar{\rho}\widetilde{u_j u_i u_i} - \bar{\rho}\tilde{u}_j\widetilde{u_i u_i}). \tag{2.9}$$

It is suggested that SGS turbulent diffusion can be approximated as $\mathcal{J}_j = \tau_{ij}\tilde{u}_i$ (Martin, Piomelli & Candler 2000). The SGS stress tensor τ_{ij} and the SGS heat flux Q_j need to be modelled based on the resolved quantities. The models for these terms are discussed below.

2.2. *Subgrid-scale model*

In LES, the eddy-viscosity model is the most commonly used SGS stress model for τ_{ij}, and it is a phenomenological model. The SGS stress tensor is modelled by a term with a structure similar to that of viscous stress. Using a subgrid viscosity μ_{sgs} to mimic the molecular viscosity, the formulation of the SGS stress τ_{ij} is written as

$$\tau_{ij}^{mod} - \tfrac{1}{3}\delta_{ij}\tau_{kk}^{mod} = -2\mu_{sgs}(\tilde{S}_{ij} - \tfrac{1}{3}\delta_{ij}\tilde{S}_{kk}). \tag{2.10}$$

The typical expression of μ_{sgs} in (2.10) is the SM (Smagorinsky 1963), which is obtained from the resolved strain-rate tensor. Then,

$$\mu_{sgs} = \bar{\rho} C_{sm} \varDelta^2 |\tilde{S}|, \tag{2.11}$$

with

$$|\tilde{S}| = \sqrt{2\tilde{S}_{ij}\tilde{S}_{ij}}, \tag{2.12}$$

and C_{sm} is the coefficient of the anisotropic part of the SM. The isotropic part of the SGS tensor is

$$\tau_{kk}^{mod} = 2C_I \bar{\rho} \varDelta^2 |\tilde{S}|^2, \tag{2.13}$$

and C_I is the coefficient of the isotropic part of the SM (Yoshizawa 1986). The SGS heat flux can be modelled as

$$Q_j^{mod} = -\frac{\mu_{sgs}}{Pr_t}\frac{\partial \tilde{T}}{\partial x_j}, \tag{2.14}$$

where Pr_t is the SGS Prandtl number.

3. Kinetic-energy-flux-constrained model (KCM)

Since the proposal of the first concept of the energy cascade by Richardson, research on the energy cascade has always been the core content of turbulence studies (Pope 2000), and it is also the most well-known statistical characteristic in LES (Moser, Haering & Yalla 2021). Kolmogorov (1941) quantitatively formulated the energy cascade for the first time

and suggested that the kinetic energy flux (KEF) is constant in the inertial subrange of locally isotropic turbulence, where the energy flux refers to the energy transfer rate from the large scale to the small scale. Subsequently, a variety of studies have focused on the KEF of incompressible and compressible turbulent flows (Meneveau & Sreenivasan 1987; Borue & Orszag 1998; Eyink 2006; Wang *et al.* 2013). The KEF between different-scale eddies is the essence of the energy cascade and reflects the dynamic process of the generation and evolution of turbulence. The accurate prediction of KEF at different scales guarantees accurate simulation of turbulent flows. At the given scale $\varDelta$, the filtered kinetic energy equation can be written as

$$\frac{\partial(\frac{1}{2}\bar{\rho}\tilde{u}_i^2)}{\partial t} + \frac{\partial}{\partial x_j}\boldsymbol{J}_\varDelta = \varPi_\varDelta + D_\varDelta + \bar{p}\frac{\partial \tilde{u}_i}{\partial x_i}, \tag{3.1}$$

$$\boldsymbol{J}_\varDelta = \tfrac{1}{2}\bar{\rho}\tilde{u}_i^2\tilde{u}_j - \tilde{u}_i\tilde{\sigma}_{ij} + \tilde{u}_i\tau_{ij} + \bar{p}\tilde{u}_j, \tag{3.2}$$

$$D_\varDelta = \tilde{\sigma}_{ij}\frac{\partial \tilde{u}_i}{\partial x_j}, \tag{3.3}$$

$$\varPi_\varDelta = \tau_{ij}\frac{\partial \tilde{u}_i}{\partial x_j}, \tag{3.4}$$

where $\boldsymbol{J}_\varDelta$ is the spatial transport of large-scale kinetic energy, $\bar{p}(\partial\tilde{u}_i/\partial x_i)$ is large-scale pressure dilatation and $D_\varDelta$ is the viscous dissipation acting on the large scale. Here, $\varPi_\varDelta$ is the KEF term from scale $\varDelta$ to the smaller scale.

In transitional and turbulent flows, on the given mesh scale $\varDelta$, the total dissipation $\varepsilon_\varDelta$ should be expressed as

$$\varepsilon_\varDelta = D_\varDelta + \varPi_\varDelta. \tag{3.5}$$

For transitional flow, laminar and turbulent flow regions coexist with irregular spatial and temporal distributions, which is also known as the phenomenon of spatiotemporal intermittency (Chaté & Manneville 1987; Tritton 2012). The KEF $\varPi_\varDelta$ through the mesh scale $\varDelta$ is approximately equal to zero in the laminar region, but it cannot be ignored in the turbulent region. In full turbulence, we consider the local KEF to exist in the whole region of the turbulent flow. In the filtered kinetic energy equation (3.1), the KEF $\varPi_\varDelta$ is an unclosed term and needs to be modelled. Based on the tensor eddy viscosity, Borue & Orszag (1998) suggested a simple parametrization for the local KEF in the inertial subrange of homogeneous and isotropic turbulence for the first time. Subsequently, Eyink (2006) developed a multiscale gradient expansion of KEF in incompressible homogeneous turbulence.

Equation (3.4) shows that the KEF is proportional to the product of the SGS stress tensor and the resolved velocity gradient tensor. To obtain a proper KEF similar to the real KEF in complex turbulent flows, a suitable SGS stress model τ_{ij} should be selected. For the SM, the KEF of scale $\varDelta$ can be expressed as

$$\varPi_\varDelta^{SM} = -2C_{sm}\bar{\rho}\varDelta^2|\tilde{S}|\left(\tilde{S}_{ij} - \tfrac{1}{3}\delta_{ij}\tilde{S}_{kk}\right)\frac{\partial\tilde{u}_i}{\partial x_j} + \tfrac{2}{3}C_I\bar{\rho}\varDelta^2|\tilde{S}|^2\delta_{ij}\frac{\partial\tilde{u}_i}{\partial x_j}, \tag{3.6}$$

and the KEF obtained from the anisotropic part $\varPi_\varDelta^{SMA}$ and the isotropic part $\varPi_\varDelta^{SMI}$ can be denoted, respectively, as

$$\varPi_\varDelta^{SMA} = -2C_{sm}\bar{\rho}\varDelta^2|\tilde{S}|(\tilde{S}_{ij} - \tfrac{1}{3}\delta_{ij}\tilde{S}_{kk})\tilde{S}_{ij} \tag{3.7}$$

and

$$\varPi_\varDelta^{SMI} = \tfrac{2}{3}C_I\bar{\rho}\varDelta^2|\tilde{S}|^2\delta_{ij}\tilde{S}_{ij}. \tag{3.8}$$

The KEF from the SM has a low correlation with the real KEF, which will cause the turbulence structure calculated from the SM to be very different from the real turbulence.

To obtain a more accurate resolved KEF, Eyink (2006) proposed the multiscale gradient expansion method for KEF, and the SGS stress can also be expressed as an expanded form totally. Through simplification, we have the approximation of the SGS stress as

$$\tau_{ij} \approx \frac{C_2}{3}\bar{\rho}\varDelta^2\frac{\partial\tilde{u}_i}{\partial x_k}\frac{\partial\tilde{u}_j}{\partial x_k}. \tag{3.9}$$

For the isotropic filter, $C_2 = 1/4$, and (3.9) can be expressed as

$$\tau_{ij} \approx \frac{1}{12}\bar{\rho}\varDelta^2\frac{\partial\tilde{u}_i}{\partial x_k}\frac{\partial\tilde{u}_j}{\partial x_k}, \tag{3.10}$$

which is the same form as the tensor-diffusivity (TD) model (Vreman, Geurts & Kuerten 1995). Then, the approximation of the KEF can be obtained as

$$\varPi_\varDelta \approx \varPi_\varDelta^{TD} = \tau_{ij}^{TD}\frac{\partial\tilde{u}_i}{\partial x_j}, \tag{3.11}$$

which has already been investigated in previous literature (Verstappen 2004; Vreman, Geurts & Deen 2004; Vreman *et al.* 2009). From (3.9)–(3.11), we know that Π_Δ^{TD} has a high correlation with the real KEF.

To obtain a more accurate KEF model, we assume that there exists a ratio η_Δ between the real KEF and the model KEF, and η_Δ is a dimensionless variable. Then, we can obtain the more precise KEF as

$$\Pi_\Delta = \Pi_\Delta^M = \eta_\Delta \tau_{ij}^{TD} \frac{\partial \tilde{u}_i}{\partial x_j}. \tag{3.12}$$

Based on the linear stability analysis of the one-dimensional Burgers equation with the TD model, Vreman *et al.* (1996) have shown that the TD model is unstable. Thus, we take the modified KEF (3.12) to constrain the SM in the LES of compressible wall-bounded turbulence, which can ensure that the LES results are highly similar to the real flow field and maintain the robustness of the computation. Hence, on the basis of the KEF constraint criterion, the following is required:

$$\Pi_\Delta^M = \Pi_\Delta^{SM}. \tag{3.13}$$

From (3.6)–(3.8), we know that

$$\Pi_\Delta^{SM} = \Pi_\Delta^{SMA} + \Pi_\Delta^{SMI}. \tag{3.14}$$

Additionally, the model KEF Π_Δ^M can be divided into two parts, one from the anisotropic part Π_Δ^{MA} and the other from the isotropic part Π_Δ^{MI}:

$$\Pi_\Delta^M = \Pi_\Delta^{MA} + \Pi_\Delta^{MI}, \tag{3.15}$$

$$\Pi_\Delta^{MA} = \eta_\Delta (\tau_{ij}^{TD} - \tfrac{1}{3}\tau_{kk}^{TD}\delta_{ij})\tilde{S}_{ij}, \tag{3.16}$$

and

$$\Pi_\Delta^{MI} = \tfrac{1}{3}\eta_\Delta \tau_{kk}^{td}\delta_{ij}\tilde{S}_{ij}. \tag{3.17}$$

Then, according to the constraint, we let $\Pi_\Delta^{MA} = \Pi_\Delta^{SMA}$ and $\Pi_\Delta^{MI} = \Pi_\Delta^{SMI}$, and the coefficients of the SM can be presented as

$$C_{sm} = -\eta_\Delta \frac{(\tau_{ij}^{TD} - \frac{1}{3}\tau_{kk}^{TD}\delta_{ij})\tilde{S}_{ij}}{2\bar{\rho}\Delta^2|\tilde{S}|(\tilde{S}_{ij} - \frac{1}{3}\delta_{ij}\tilde{S}_{kk})\tilde{S}_{ij}}, \tag{3.18}$$

$$C_I = \eta_\Delta \frac{\tau_{kk}^{TD}\delta_{ij}\tilde{S}_{ij}}{2\bar{\rho}\Delta^2|\tilde{S}|^2\delta_{ij}\tilde{S}_{ij}}. \tag{3.19}$$

Thus, the new KCM has been proposed in this way, and the ratio η_Δ between the real KEF and the KEF from the TD model is the key variable in the KCM, which can be obtained by the ANN method.

4. Artificial neural network

In this work, we use an ANN to construct the relation between the input features and the ratio η_Δ in compressible wall turbulence. For compressible wall turbulence, compressible turbulent channel flow is the simplest case; it reflects the main characteristics of compressible wall-bounded turbulence and has also been deeply studied theoretically (Coleman, Kim & Moser 1995; Foysi, Sarkar & Friedrich 2004; Morinishi, Tamano &

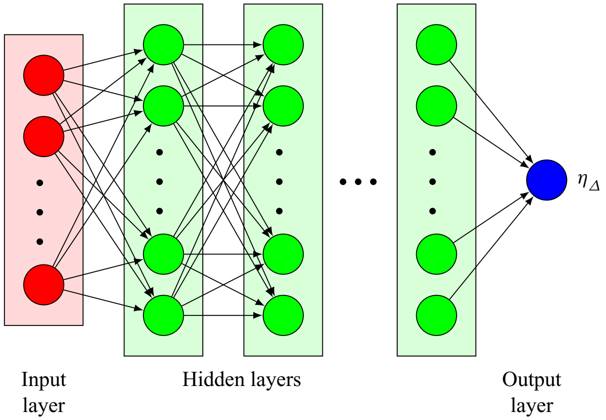

Figure 1. Schematic diagram of the ANN for predicting the KEF ratio $\eta_\varDelta$.

Nakabayashi 2004; Ghosh, Foysi & Friedrich 2010; Li *et al.* 2019). The data selected for training and testing in this study are obtained from the DNS data of a temporally compressible isothermal-wall turbulent channel flow (Coleman *et al.* 1995). For this flow, the Mach number $Ma = 1.5$, the Reynolds number $Re = 3000$ and the friction Reynolds number $Re_\tau = u_\tau\delta/\nu = 220$ (where u_τ and δ are the friction velocity and the half-width of the channel). The computational domain for the DNS of channel flow is a box with a size of $4\pi \times 2 \times \frac{4}{3}\pi$, and the grids for DNS are $900 \times 201 \times 300$ and $\Delta x^+ \times \Delta y^+_{wall} \times \Delta z^+ = 3 \times 0.32 \times 3$, where Δx^+, Δy^+_{wall} and Δz^+ ($\Delta x_i^+ = \Delta x_i u_\tau/\nu$) are the mesh spacings (wall units) in the streamwise, wall-normal and spanwise directions. During the course of training and testing, the DNS data are filtered in the streamwise and spanwise directions with a top-hat filter.

The schematic diagram of the ANN is shown in figure 1. The ANN is composed of multiple layers with many neurons. The neurons receive the input signals from the previous layer and send them to the next layer by the successive mathematical operation of the linear weighted sum and nonlinear activation. Each neuron in the lth layer receives the inputs $X_j^{(l-1)}$ from the $(l-1)$th layer and then transmits them to the outputs $X_i^{(l)}$ activated by the nonlinear function. The transfer function from the $(l-1)$th layer to the lth layer is calculated as

$$X_i^{(l)} = \sigma\left[b_i^{(l)} + \sum_j W_{ij}^{(l)} X_j^{(l-1)}\right], \tag{4.1}$$

where $\sigma[\cdot]$ is the nonlinear activation function and $W_{ij}^{(l)}$ and $b_i^{(l)}$ are the weights and biases in the lth layer, respectively.

The input features of the ANN are critical to the performance of predicting the KEF ratio $\eta_\varDelta$. A set of input variables is listed in table 1 for different ANN models. The input variables for ANN models are dimensionless quantities, where several variables may be selected in compressible wall-bounded turbulence, such as $\varDelta^+$, y^+, $Re_\varDelta$ and $\varDelta_\ell^+$. In this paper, $\varDelta^+ = \bar\rho_w \tilde u_\tau \varDelta/\mu_w$ is the normalized filter width, $y^+ = \bar\rho_w \tilde u_\tau y/\mu_w$ is the dimensionless normal distance, $Re_\varDelta = \bar\rho_w |\tilde S| \varDelta^2/\mu_w$ is the mesh Reynolds number and $\varDelta_\ell^+ = \varDelta/\ell$, with $\ell = [\mu_w^3/(\bar\rho_w^3 \varepsilon)]^{1/4} = [\mu_w^2/(2\bar\rho_w^2 \langle \tilde S_{ij}\tilde S_{ij}\rangle)]^{1/4}$. Here, $\tilde u_\tau = \sqrt{\tau_w/\bar\rho_w}$ is the filtered wall friction velocity, where $\tau_w = \mu_w(\partial \tilde u/\partial y)$ is the wall shear stress, and $\langle\cdot\rangle$

Model	ANN1	ANN2	ANN3	ANN1-SL	ANN2-SL	ANN3-SL
Inputs	$\{\Delta^+, y^+\}$	$\{\Delta_\ell^+, y^+\}$	$\{Re_\Delta, y^+\}$	$\{\Delta_{SL}^+, y_{SL}^+\}$	$\{\Delta_{\ell,SL}^+, y_{SL}^+\}$	$\{Re_{\Delta,SL}, y_{SL}^+\}$
Outputs	$\{\eta_\Delta\}$	$\{\eta_\Delta\}$	$\{\eta_\Delta\}$	$\{\eta_\Delta\}$	$\{\eta_\Delta\}$	$\{\eta_\Delta\}$
M (no. inputs)	2	2	2	2	2	2

Table 1. A set of inputs and outputs for different ANN models.

denotes the spatial average along the homogeneous directions. In table 1, ANN1, ANN2 and ANN3 are the ANN models with input parameters normalized by the wall quantities (i.e. ρ_w and μ_w).

Apart from the dimensionless physical variables normalized by the wall quantities, we also select the dimensionless quantities using the semi-local normalization (Pecnik & Patel 2017; Yang & Lv 2018) as the input features of the ANN. The corresponding semi-local (SL) scaled variables include Δ_{SL}^+, y_{SL}^+, $Re_{\Delta,SL}$ and $\Delta_{\ell,SL}^+$. Here, the semi-local scaled filter width is defined by $\Delta_{SL}^+ = \bar{\rho}\tilde{u}_\tau\Delta/\mu$, $y_{SL}^+ = \bar{\rho}\tilde{u}_\tau y/\mu$ is the semi-local scaled normal distance, $Re_{\Delta,SL} = \bar{\rho}|\tilde{S}|\Delta^2/\mu$ is the local mesh Reynolds number and $\Delta_{\ell,SL}^+ = \Delta/\ell_{SL}$, where $\ell_{SL} = [\mu^3/(\bar{\rho}^3\varepsilon)]^{1/4} = [\mu^2/(2\bar{\rho}^2\langle\tilde{S}_{ij}\tilde{S}_{ij}\rangle)]^{1/4}$. Then, ANN1-SL, ANN2-SL and ANN3-SL represent the ANN models with input variables normalized by the semi-local physical quantities in table 1.

A total of four layers (an input layer, two hidden layers and an output layer) with neurons in the ratio $M : 100 : 100 : 1$ are chosen in this paper, where M is the number of input variables listed in table 1. The activation functions of the hidden layers and output layer are the hyperbolic tangent function (tanh) and linear function, respectively, which are defined by

$$\sigma_h(x) = \frac{\mathrm{e}^x - \mathrm{e}^{-x}}{\mathrm{e}^x + \mathrm{e}^{-x}}, \quad \sigma_o(x) = x. \tag{4.2}$$

The mean-squared error (MSE) function is selected as the loss function of the ANN, which is defined as $L = \langle(\eta_\Delta^{true} - \eta_\Delta^{pred})^2\rangle$, where η_Δ^{true} and η_Δ^{pred} denote the true and predicted values of the ANN, respectively. A total of 2×10^4 samples are selected from 20 snapshots of the filtered DNS data with a ratio of the filter width Δ/Δ_{DNS} ranging from 2 to 20 (i.e. $\Delta/\Delta_{DNS} \in \{2, 4, \ldots, 20\}$). We use the cross-validation strategy and divide the dataset into a training set and a testing set to suppress parameter overfitting of the ANN; 70 % of the samples are randomly extracted from the total dataset and are used as the training set, while the others are used for testing. The weights of the ANN are initialized by the Glorot-uniform algorithm and optimized by the Adam algorithm (Kingerma & Ba 2019) for 1×10^4 iterations, with a batch size and learning rate of 1000 and 0.01, respectively. The grid search method is chosen as the hyperparameter pruning method of the ANN to determine the optimal hyperparameters, such as the numbers of layers and neurons and the types of activation functions. The learning curves of the ANN models for different input variables using different normalization methods are shown in figure 2. After a long training with 1×10^4 epochs, the MSE losses in both the training sets and testing sets converge quickly and gradually reach stationarity. The training loss and testing loss for both wall quantity normalization and semi-local scaling methods are very close, which means that the selected hyperparameters are reasonable and all the ANN models are well trained.

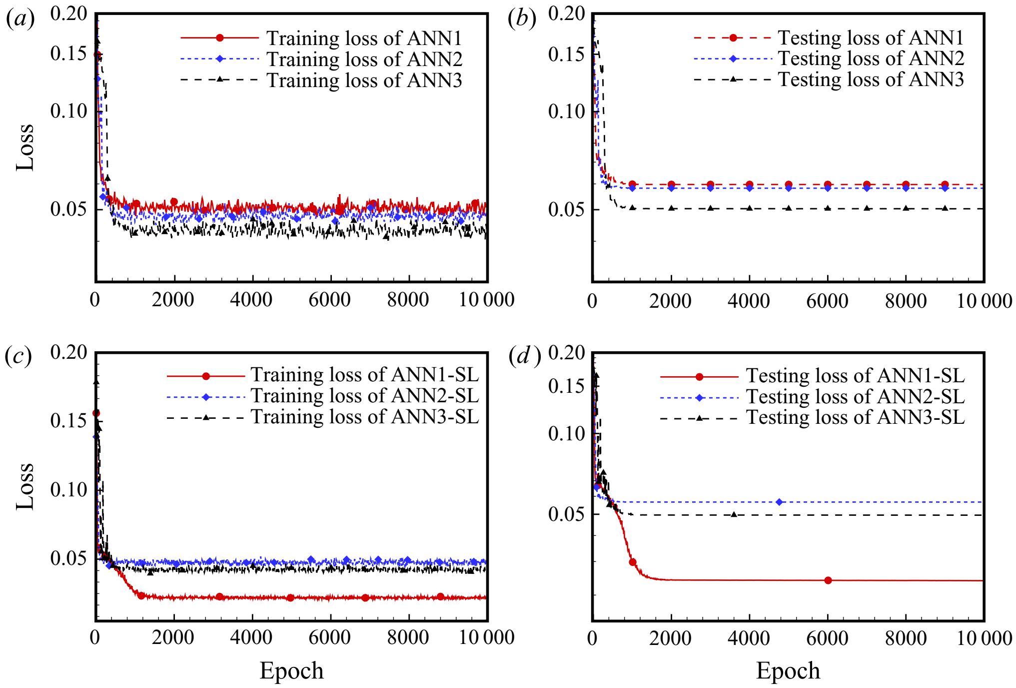

Figure 2. Learning curves of the proposed ANN models for predicting the KEF ratio η_Δ: (*a*) training loss for ANN models, (*b*) testing loss for ANN models, (*c*) training loss for ANN-SL models and (*d*) testing loss for ANN-SL models.

We evaluate the performance of different ANN models by calculating three metrics to measure the difference between the true value (η_Δ^{real}) obtained from the filtered DNS data and the predicted value (η_Δ^{model}) calculated by the ANN models. They are the correlation coefficient $C(\eta_\Delta)$, the relative error $E_r(\eta_\Delta)$ and the ratio of the root-mean-square value $R(\eta_\Delta)$, which are expressed, respectively, as

$$C(\eta_\Delta) = \frac{\langle(\eta_\Delta^{real} - \langle\eta_\Delta^{real}\rangle)(\eta_\Delta^{model} - \langle\eta_\Delta^{model}\rangle)\rangle}{\langle(\eta_\Delta^{real} - \langle\eta_\Delta^{real}\rangle)^2\rangle^{1/2}\langle(\eta_\Delta^{model} - \langle\eta_\Delta^{model}\rangle)^2\rangle^{1/2}}, \tag{4.3}$$

$$E_r(\eta_\Delta) = \frac{\langle(\eta_\Delta^{real} - \eta_\Delta^{model})^2\rangle^{1/2}}{\langle(\eta_\Delta^{real})^2\rangle^{1/2}}, \tag{4.4}$$

$$R(\eta_\Delta) = \frac{\langle(\eta_\Delta^{model} - \langle\eta_\Delta^{model}\rangle)^2\rangle^{1/2}}{\langle(\eta_\Delta^{real} - \langle\eta_\Delta^{real}\rangle)^2\rangle^{1/2}}. \tag{4.5}$$

The results with high correlation coefficients, low relative errors and high ratios of root-mean-square values indicate successful modelling.

Table 2 shows comparisons of the correlation coefficients, relative errors and ratios of root-mean-square values for the KEF ratio η_Δ in both training and testing sets after the 10 000-iteration training process. The results of the training and testing sets show slight differences, which indicates that none of the trained ANN models with different inputs are overfitted. Furthermore, the metrics predicted by the semi-local normalization

Dataset\	ANN1	ANN2	ANN3	ANN1-SL	ANN2-SL	ANN3-SL
$C(\eta_\Delta)$						
Training set	0.9160	0.9207	0.9287	0.9647	0.9216	0.9306
Testing set	0.9061	0.9087	0.9215	0.9568	0.9130	0.9226
$E_r(\eta_\Delta)$						
Training set	0.1261	0.1227	0.1166	0.0828	0.1220	0.1150
Testing set	0.1367	0.1349	0.1255	0.0941	0.1318	0.1246
$R(\eta_\Delta)$						
Training set	0.9115	0.9201	0.9229	0.9526	0.9188	0.9280
Testing set	0.8931	0.9044	0.9109	0.9375	0.9045	0.9153

Table 2. Correlation coefficient (C), relative error (E_r) and ratio of root-mean-square value (R) of the KEF ratio η_Δ in different datasets for different ANN models.

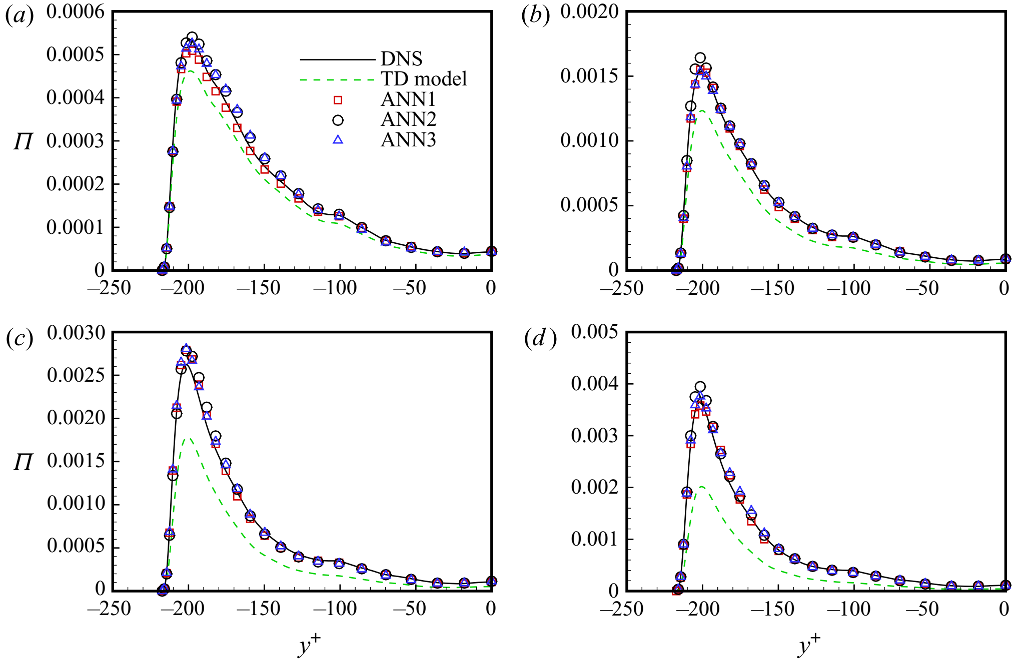

Figure 3. Comparisons of the KEF reconstructed by different ANN models using wall-quantity normalization along the normal direction with different filter widths: (*a*) $\Delta/\Delta_{DNS} = 4$; (*b*) $\Delta/\Delta_{DNS} = 8$; (*c*) $\Delta/\Delta_{DNS} = 12$; and (*d*) $\Delta/\Delta_{DNS} = 16$.

obviously outperform those normalized by the wall quantities, especially for the case of ANN1-SL. The ANN1-SL model performs better than the other five ANN models. The correlation coefficient and relative error of the ANN1-SL model in the testing dataset are 96 % and 9.4 %, respectively. The ratio of the root-mean-square value of the ANN1-SL model is equal to 0.94 and very close to 1, which indicates that the ANN1-SL model can accurately reconstruct the KEF ratio. In contrast to other ANN models, we take the local mesh Reynolds number instead of the normalized filter width in the input of the ANN1-SL model. The prediction performance improves to some degree. More importantly, ANN1-SL can be more easily generalized to other types of compressible wall-bounded turbulence.

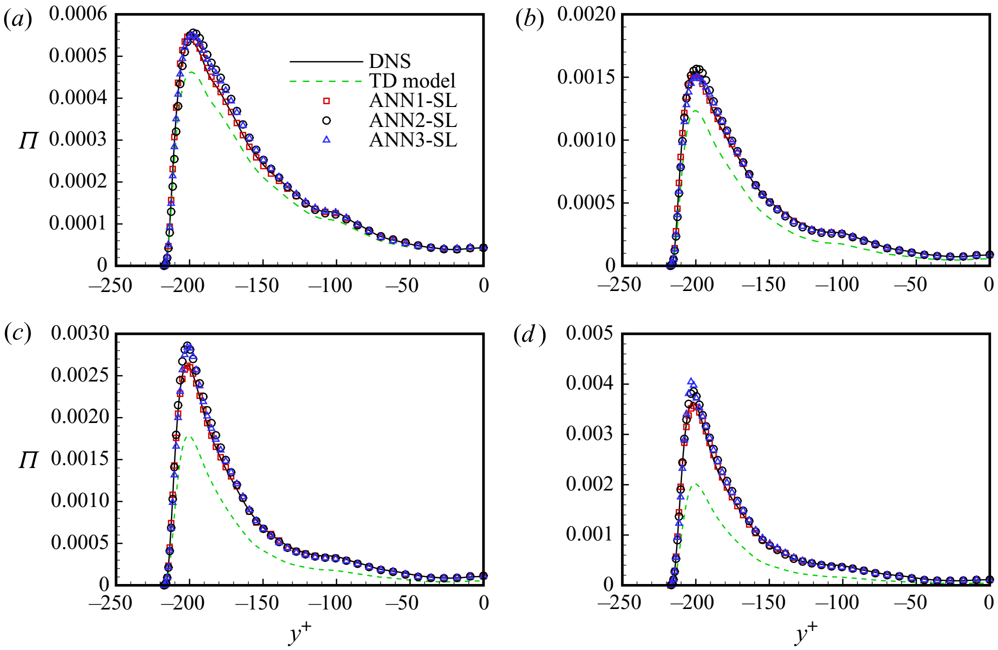

Figure 4. Comparisons of the KEF reconstructed by different ANN models using semi-local normalization with different filter widths: (*a*) $\varDelta/\varDelta_{DNS} = 4$; (*b*) $\varDelta/\varDelta_{DNS} = 8$; (*c*) $\varDelta/\varDelta_{DNS} = 12$; and (*d*) $\varDelta/\varDelta_{DNS} = 16$.

Comparisons of the KEF reconstructed by different ANN models and that from the TD model along the normal direction with different filter widths ($\varDelta/\varDelta_{DNS} = 4$, 8, 12, 16) are shown in figures 3 and 4. The magnitudes of the KEF obtained from the TD model with these filter widths are obviously different from the real value, even though their shapes are very similar due to the high correlation coefficients. The KEF modelled by the ANN models is very close to the DNS data, and the six ANN models show similar results. Since the ANN1-SL model demonstrates the better *a priori* accuracy among these ANN models, we can also use the ANN1-SL model to reconstruct the KEF ratio $\eta_\varDelta$ in the KCM as the representation of these ANN models. The newly constructed KEF model here is a semi-explicit model.

5. Results of applications

5.1. *Application in compressible turbulent channel flows*

In this section, the KCM will be verified in compressible turbulent channel flows, and the case setting of the LES is the same as that of the DNS in § 4. The filtered Navier–Stokes equations (2.1)–(2.3) are solved using a high-precision non-dimensional finite-difference solver in Cartesian coordinates: the equations are temporally integrated using the third-order Runge–Kutta scheme, and a sixth-order central-difference scheme is used for the discretization of both the convective and viscous terms.

In this study, we will select three commonly used SGS models for comparison, namely the Vreman model, WALE model and DSM. In the DSM, C_{sm}, C_I and Pr_T are solved dynamically based on the Germano identity. Following the form of the Vreman model in compressible turbulence (Sayadi & Moin 2012; Zhang, Wan & Sun 2019), the model coefficient $C_v = 2.5C_{sm}^2$, where $C_{sm} = 0.1$. The WALE model here is taken in the same

	Grids	$\varDelta x^+$	$\varDelta y_w^+$	$\varDelta z^+$
DNS	$900 \times 201 \times 300$	2.99	0.32	2.99
Smagorinsky	$48 \times 65 \times 48$	54.32	1.01	18.11
Vreman	$48 \times 65 \times 48$	56.48	1.05	18.83
WALE	$48 \times 65 \times 48$	54.86	1.02	18.28
DSM	$48 \times 65 \times 48$	57.55	1.07	19.18
KCM	$48 \times 65 \times 48$	57.55	1.07	19.18

Table 3. Parameters of the simulations in compressible channel flow ($Ma = 1.5$, $Re = 3000$, $Re_\tau = 220$).

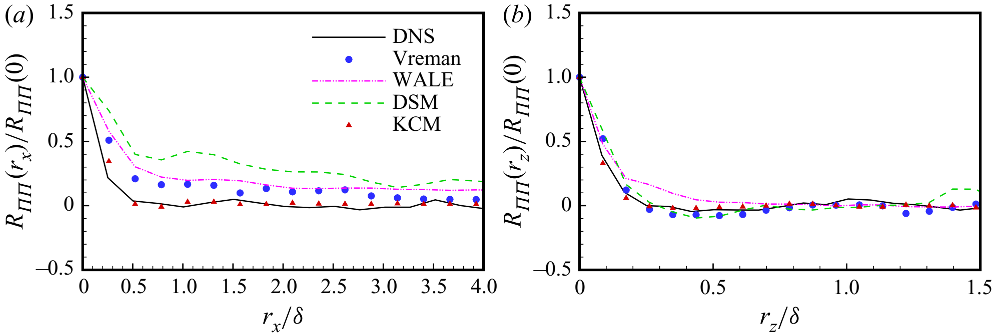

Figure 5. Two-point correlation coefficients of KEF at various locations of $y^+ = 50$: (*a*) streamwise correlation; and (*b*) spanwise correlation. DNS (black solid line), Vreman (blue circles), WALE (pink dash-double dotted line), DSM (green dashed line) and KCM (red triangles).

form as in Garnier, Adams & Sagaut (2000). The model coefficient of WALE is $C_w = 10.6C_{sm}^2$, and C_{sm} is also taken as 0.1. In Garnier *et al.* (2000), Sayadi & Moin (2012) and Zhang *et al.* (2019), the isotropic parts of the Vreman and WALE models are ignored, and we also adopt $C_I = 0$ for the Vreman and WALE models here. The SGS Prandtl number Pr_T of the Vreman model, WALE model and KCM can be evaluated as 0.9 empirically (Georgiadis, Alexander & Reshotko 2001; Sayadi & Moin 2012; Zhang *et al.* 2019). The filtering procedure is also performed using a top-hat filter. The grid filter width is $\varDelta = (\varDelta_x\varDelta_y\varDelta_z)^{1/3}$, with $\varDelta_x$, $\varDelta_y$ and $\varDelta_z$ representing the local grid width along the three axes, and the test-filter width is set as $2\varDelta$. But the Vreman model is implemented using the filter width in each direction according to its model form. The details of the grid settings are listed in table 3.

Spatial correlation coefficients of KEF can reveal the prediction ability of SGS models on the spatial structures of KEF. Figure 5(*a*,*b*) shows the streamwise and spanwise two-point correlation coefficients of KEF at various locations of $y^+ = 50$, respectively. The two-point correlation coefficient of KEF can be defined as

$$R_{\varPi\varPi}(\boldsymbol{r}) = \frac{\varPi(\boldsymbol{x})\varPi(\boldsymbol{x}+\boldsymbol{r})}{\varPi(\boldsymbol{x})\varPi(\boldsymbol{x})}. \tag{5.1}$$

From figure 5, we can see that both the streamwise and spanwise two-point correlation coefficients of KEF from KCM are much closer to the real values than other models, indicating that KCM gives a good modelling of the main spatial distribution characteristics of KEF.

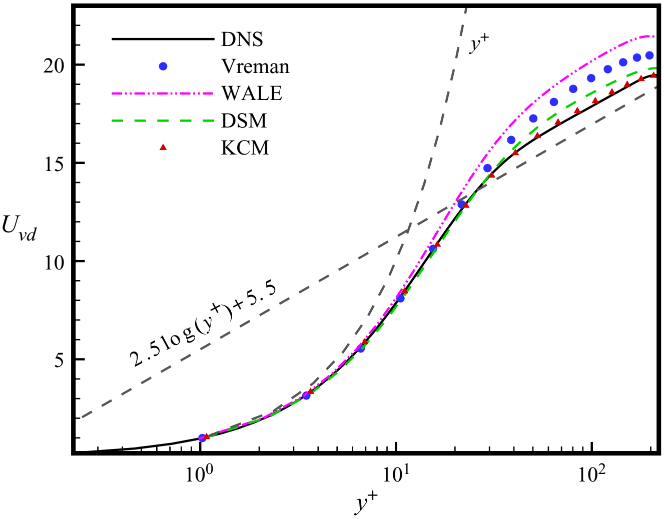

Figure 6. Van Driest transformed mean velocity files from different SGS and result from DNS for comparison.

The distribution of the van Driest transformed mean streamwise velocity ($U_{vd} = \int_0^U \sqrt{\langle\rho\rangle/\rho_w}\, \mathrm{d}\langle U\rangle$) as a function of y^+ is displayed in figure 6, and the results obtained from DNS, KCM and some representative eddy-viscosity models, including DSM, Vreman and WALE (Germano *et al.* 1991; Nicoud & Ducros 1999; Vreman 2004) are compared together. As expected for $y^+ < 5$, the mean streamwise velocity generally increases linearly with y^+. Additionally, almost all the results from the SGS models collapse to the DNS result in the viscous sublayer and up to part of the buffer region ($y^+ < 20$). In the log-law region, the KCM still provides a perfect estimation of U_{vd}, but the results of other SGS models show an obvious deviation from the DNS result. Furthermore, from figure 6, we know that the KCM provides proper SGS dissipation, but the other typical eddy-viscosity SGS models exhibit excessive SGS dissipation.

Figure 7(*a*)–(*c*) shows the profiles of the normalized resolved turbulence intensities $\tilde{u}_i^{rms}/u_\tau = \langle(\tilde{u}_i - \langle\tilde{u}_i\rangle)^2\rangle^{1/2}/u_\tau$ calculated from the LES data of several SGS models, including Vreman, WALE, DSM and KCM, and the result from DNS is also provided for comparison. Figure 7(*a*) shows the streamwise turbulence intensity U^{rms}, and we can see that the result of the KCM is obviously in better agreement with the DNS result than the results of the other models, especially in the buffer region. Additionally, the wall-normal turbulence intensity V^{rms} and spanwise turbulence intensity W^{rms} are shown in figure 7(*b*,*c*), respectively. As seen from the two panels, all the SGS models have low performance, but the results of KCM have a slight advantage over those of the other SGS models. Figure 7(*d*) shows the distribution of the normalized Reynolds stress R_{uv} along the normal height y^+, and the results of DNS, Vreman, WALE, DSM and KCM are compared together. The Reynolds stress can be expressed as

$$R_{ij} = \langle\rho\rangle(\{u_i u_j\} - \{u_i\}\{u_j\}), \tag{5.2}$$

where $\{\cdot\}$ denotes the Favre averaging and $\{\phi\} = \langle\rho\phi\rangle/\langle\rho\rangle$.

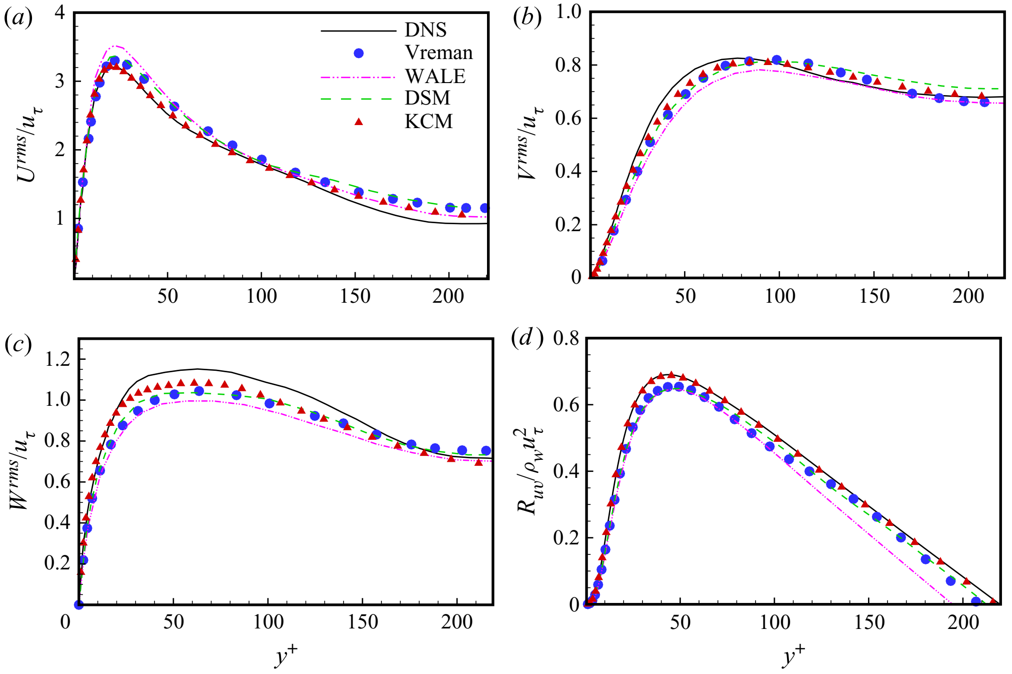

Figure 7. Turbulence intensities and the Reynolds stress normalized by the friction velocity u_τ from DNS and different models: (*a*) streamwise turbulence intensity; (*b*) wall-normal turbulence intensity; (*c*) spanwise turbulence intensity; and (*d*) Reynolds stress.

For turbulent flows, the property of ergodicity is assumed, and thus $\langle\phi\rangle = \langle\bar{\phi}\rangle$. Then, the Reynolds stress can also be expressed as

$$R_{ij} = \langle\bar{\rho}\rangle(\{\widetilde{u_i u_j}\} - \{\tilde{u}_i\}\{\tilde{u}_j\}) = R_{ij}^{LES} + \langle\tau_{ij}\rangle, \tag{5.3}$$

where

$$R_{ij}^{LES} = \langle\bar{\rho}\rangle(\{\tilde{u}_i\tilde{u}_j\} - \{\tilde{u}_i\}\{\tilde{u}_j\}) \tag{5.4}$$

is the resolved Reynolds stress and τ_{ij} is the SGS stress.

In contrast to the results of other SGS models, the KCM gives a perfect total Reynolds stress R_{uv} in almost all of the regions. The results in figure 7 demonstrate that the KCM can also better predict the high-order statistics of turbulence.

The mean temperature obtained from DNS and the four SGS models are also compared together in figure 8. KCM shows the best behaviour, and the result from Vreman is better than those of the other two models. Figure 9 displays the profiles of the normalized resolved temperature fluctuation $\tilde{T}^{rms}/T_\tau = \langle(\tilde{T} - \langle\tilde{T}_i\rangle)^2\rangle^{1/2}/T_\tau$ along the wall-normal direction from DNS and these SGS models, where $T_\tau = q_w/\rho_w c_p u_\tau$, with $q_w = -k(\partial\tilde{T}/\partial y)$ the friction temperature. The result of KCM is very close to the real value, and is better than those of other models. The temperature–velocity correlation can be written as

$$R_{u_iT} = \langle\bar{\rho}\rangle(\{\widetilde{u_iT}\} - \{\tilde{u}_i\}\{\tilde{T}\}) = R_{u_iT}^{LES} + \langle Q_i\rangle, \tag{5.5}$$

where

$$R_{u_iT}^{LES} = \langle\bar{\rho}\rangle(\{\tilde{u}_i\tilde{T}\} - \{\tilde{u}_i\}\{\tilde{T}\}) \tag{5.6}$$

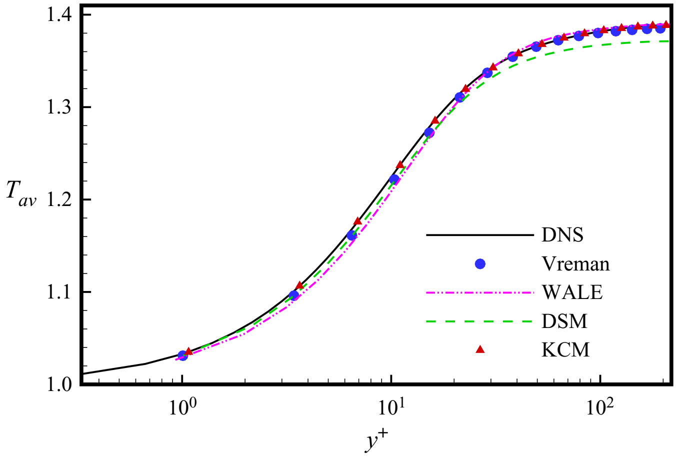

Figure 8. Mean temperature profiles obtained from DNS and different SGS models.

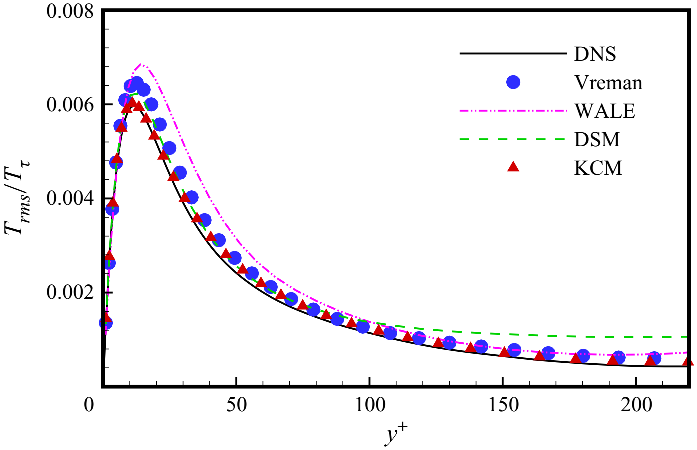

Figure 9. Temperature fluctuation normalized by friction temperature T_τ from DNS and different SGS models.

is the resolved temperature–velocity correlation and Q_i is the SGS heat flux. We show the normalized temperature–velocity correlation in figure 10, and we find that the result from KCM is much closer to the real value compared with other traditional eddy-viscosity SGS models. Thus, the reasonable eddy viscosity of KCM will improve the prediction of the SGS heat-flux model.

Accurate prediction of turbulent structure is also an important ability for the new SGS model. We show in figure 11(a–d) the instantaneous isosurface of Q (second invariant of the strain-rate tensor, $Q = 0.2$) obtained from Vreman, WALE, DSM and KCM, respectively. Comparing the four pictures, we find that the result of the KCM shows more small-scale and abundant structures, especially in the near-wall region. Nevertheless, the results of the other models show larger tube-like structures and lack small-scale structures. These observations also indicate that the KCM has the advantage of accurately predicting the turbulent structure.

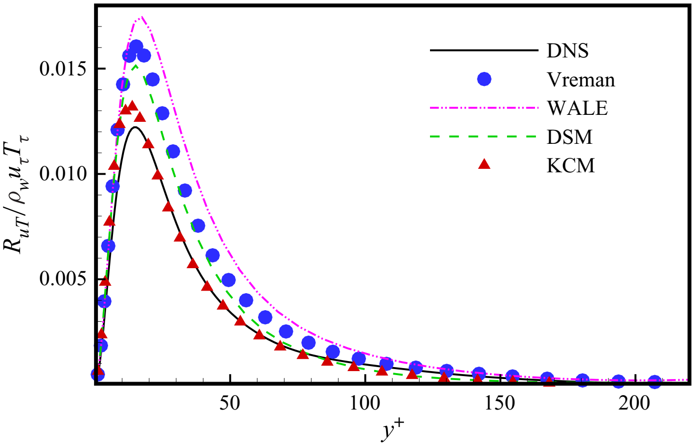

Figure 10. Normalized temperature velocity correlation from DNS and different SGS models.

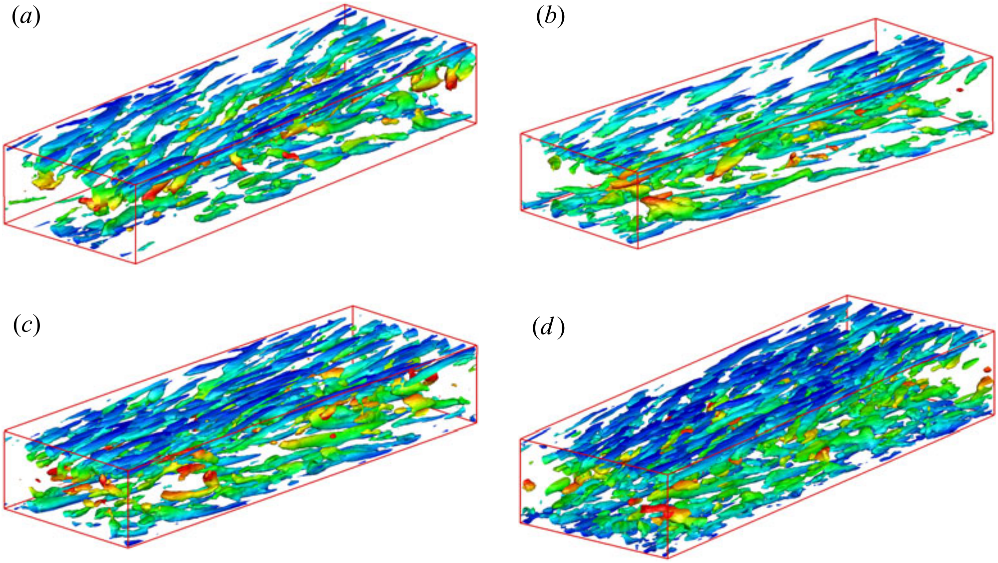

Figure 11. Instantaneous isosurface of Q (second invariant of the strain-rate tensor, $Q = 0.2$) obtained from (*a*) Vreman, (*b*) WALE, (*c*) DSM and (*d*) KCM in compressible turbulent channel flow.

Then, we need to check the performance of the KEF ratio and the model coefficients in an *a posteriori* test of compressible turbulent channel flow. Figure 12 shows the KEF ratio η_Δ of KCM in the compressible turbulent channel flow; η_Δ is almost constant for $y^+ < 120$, and the value is approximately 1.16. For $y^+ > 120$, it will grow slowly. Figure 13(*a*,*b*) displays the model coefficients C_{sm} and C_I, respectively. It is shown that the curves of C_{sm} and C_I are similar to each other. They grow rapidly from zero near the wall, and remain nearly constant in the centre region of the channel.

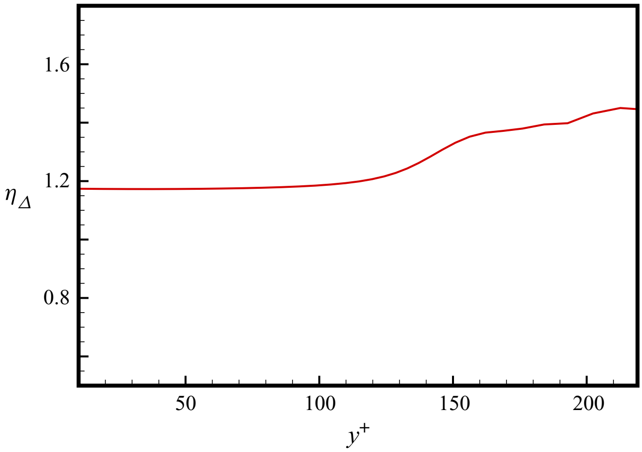

Figure 12. An *a posteriori* test of KEF ratio η_Δ of KCM in compressible channel flow.

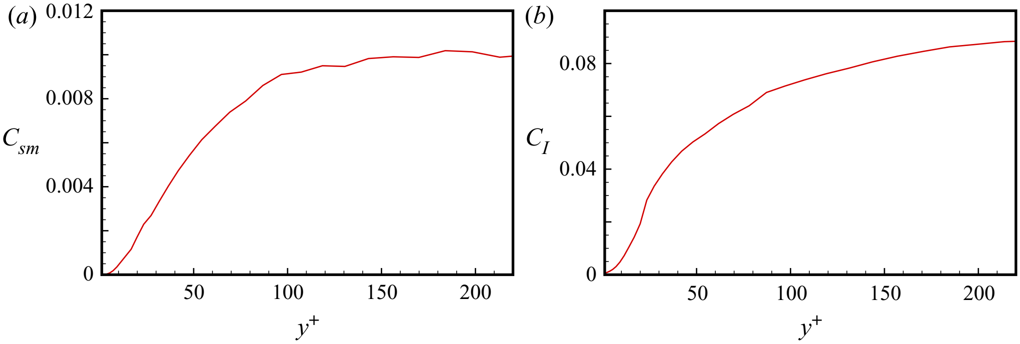

Figure 13. An *a posteriori* test of the model coefficients of KCM in compressible turbulent channel flow: (*a*) C_{sm} and (*b*) C_I.

5.2. *Application in compressible flat-plate boundary layer*

To verify the KCM in simulating more complex compressible wall flow, we select the compressible flat-plate boundary layer as a typical example. Compared with the channel flow, the flat-plate boundary layer is a more complicated type of wall-bounded flow. Flat-plate boundary layer flow is a typical flow consisting of laminar, transitional and fully turbulent regions, which is a common phenomenon in wall flow. Thus, it can be regarded as a classical case for evaluating the performance of the new SGS model in transitional and turbulent flows. The LES of the transition to turbulence of the flat-plate boundary layer has been frequently investigated over an extended period (Ducros, Comte & Lesieur 1996; Huai *et al.* 1997; Sayadi & Moin 2012).

In this paper, we choose a spatially developing supersonic adiabatic flat-plate boundary layer flow (Pirozzoli, Grasso & Gatski 2004) (at $Ma = 2.25$ and $Re_\theta \approx 4000$) to test the new model; a sketch of the computational domain for the numerical simulation is shown in figure 14. The computational domain (see figure 14) is bounded by in-flow and out-flow boundaries, a wall boundary, a far-field boundary and the two boundaries (periodic) in the spanwise direction; the computational domain has a size of $L_x \times L_y \times L_z = 6 \times 0.3 \times 0.175$. Blowing and suction disturbances are imposed at the wall with an

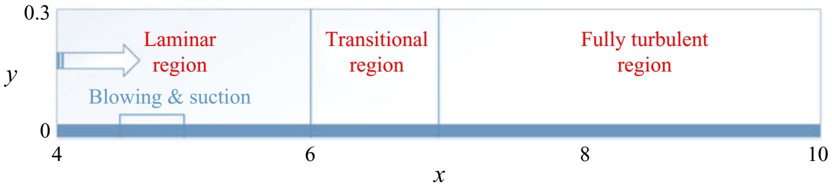

Figure 14. Sketch of the computational domain of the flat-plate boundary layer for the numerical simulation.

interval of x ($4.5 \leq x \leq 5.0$). The form of blowing and suction is the same as that in (Pirozzoli *et al.* 2004) except for the magnitude of the amplitude. To simulate a natural transition, an amplitude of 0.02 is selected in this case. The grid resolution for the DNS of this example case is $10\,090 \times 90 \times 320$, and $\Delta x^+ \times \Delta y^+ \times \Delta z^+ = 6.02 \times 0.58 \times 5.47$ in the streamwise, wall-normal and spanwise directions.

The newly proposed LES model KCM is tested *a priori* using the DNS data of the compressible flat-plate flow first. To directly explain the difference between the KEF constrained eddy-viscosity model KCM and the traditional eddy-viscosity models (i.e. the SM, WALE model, etc.) on the prediction of the spatial distribution of KEF, *a priori* tests of the energy fluxes obtained from KCM, SM, DSM, Vreman and WALE and the real value are compared in figure 15. In the *a priori* tests, the DNS data of the transition to the turbulence region at $y^+ = 15$, which is in the buffer region, are filtered in the spanwise direction with a top-hat filter, and the filter width is $\bar{\Delta} = 8\Delta_z$. From figure 15, we find that the spatial distribution of KEF obtained from the KCM is very similar to that of the real value in terms of both phase and amplitude. In contrast, the KEF distributions obtained from the other three traditional eddy-viscosity models and DSM have a significant difference from the real KEF distribution. Except for the weak negative KEF in the result from DSM, there are not any backscatters in the results from other traditional eddy-viscosity models. This result indicates that the strong ability of the KCM on the accurate prediction of KEF is valid for the transition and turbulence of the flat-plate boundary layer.

Then, for the *a posteriori* test, the numerical scheme is the same as that for the LES of the turbulent channel flow in § 5.1. In this case, we choose two sets of grids for the LES of the compressible flat-plate boundary layer; the parameter settings are shown in table 4. In figure 16, we show the distributions of the skin-friction coefficients obtained from Vreman, WALE, DSM and KCM compared with the results obtained from DNS on the two sets of grids. In figure 16, from the curve of the real skin-friction coefficient, we can see that the occurrence of the transition is at $x \approx 6.3$, the transition peak is reached at $x \approx 7.2$, and then the steady turbulence region is gradually approached as the boundary layer flow develops into fully developed turbulence. It is easy to see that all the models can predict the point of transition properly in figure 16(*a*); however, the result of the KCM still has a small advantage compared with the other results. Under the coarser grid, we find that the KCM still predicts the transition point and transition peak well, as shown in figure 16(*b*), and it has an obvious advantage compared with the other models. The traditional wall-bounded turbulence model cannot predict the transition (Sayadi & Moin 2012; Zhou *et al.* 2019*a*), but the SM constrained by KEF (KCM) can predict laminar, transitional and turbulent flow regions accurately and can provide appropriate SGS dissipation in different flow regions. The primary reason for this observation is that the KCM can supply the proper KEF in different regions.

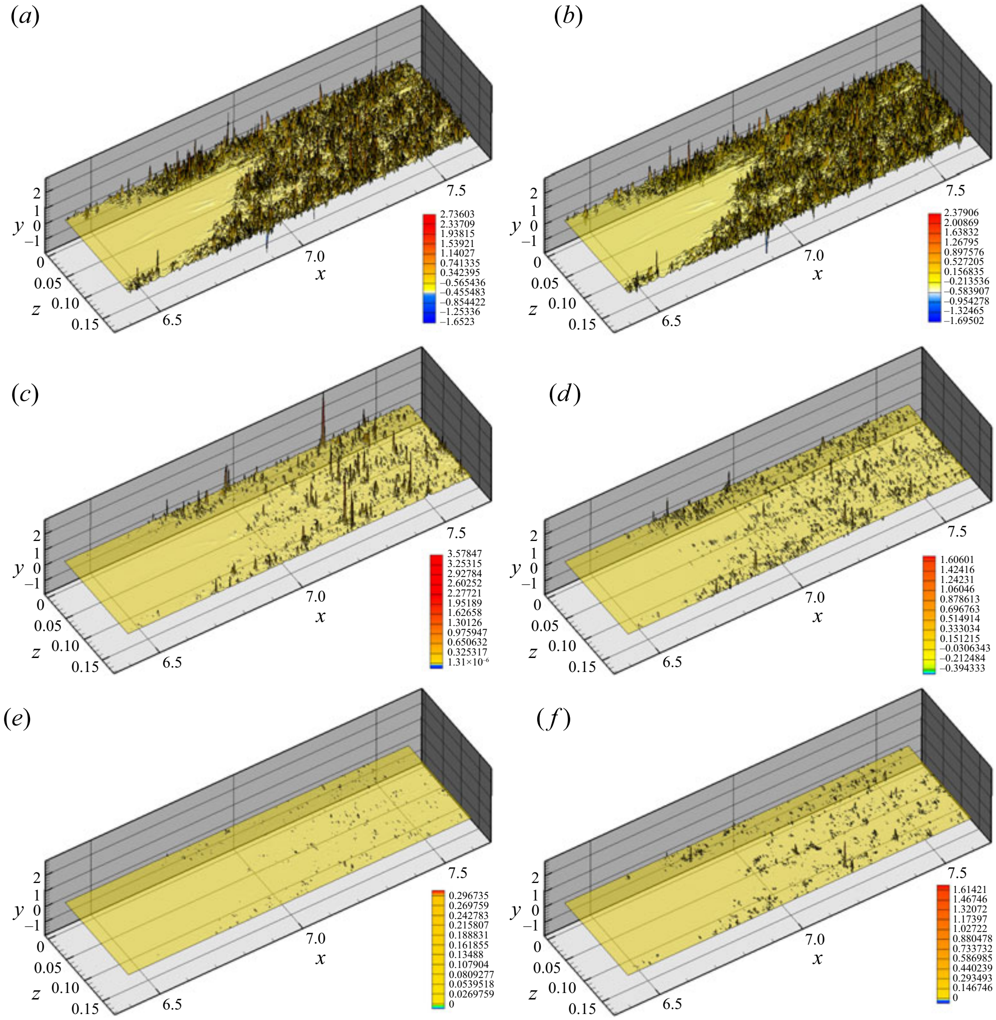

Figure 15. An *a priori* test of the local KEF of the compressible flat-plate boundary layer at $y^+ = 15$ from different SGS models, and the real value for comparison: (*a*) the real value; (*b*) KCM; (*c*) SM; (*d*) DSM; (*e*) Vreman; and (*f*) WALE.

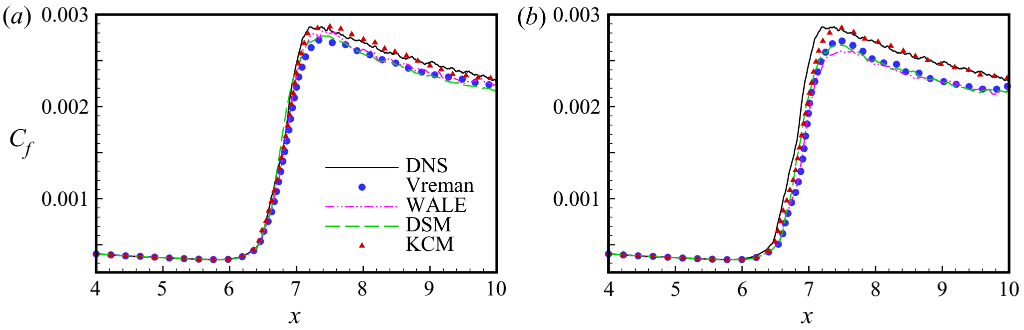

Figure 16. Skin-friction coefficient distribution along the flat plate: (*a*) grid-1 and (*b*) grid-2.

Case	N_x	N_y	N_z	Δx^+	Δy_w^+	Δz^+
DNS	10 000	90	320	6.0	0.58	5.47
LES-grid1	1500	90	100	40.1	0.58	17.5
LES-grid2	1000	90	80	60.2	0.58	21.9

Table 4. Parameters of the simulations in the supersonic transition and turbulent flat-plate boundary layer ($Ma = 2.25$, $Re = 635\,000$).

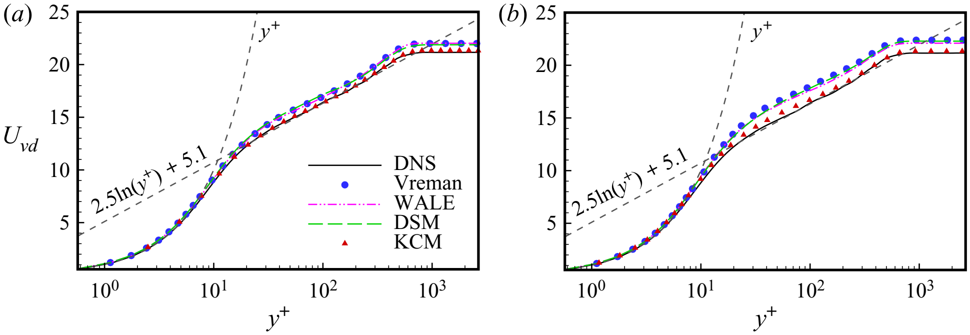

Figure 17. Van Driest transformed mean streamwise velocity at $x = 8.8$: (*a*) grid-1 and (*b*) grid-2.

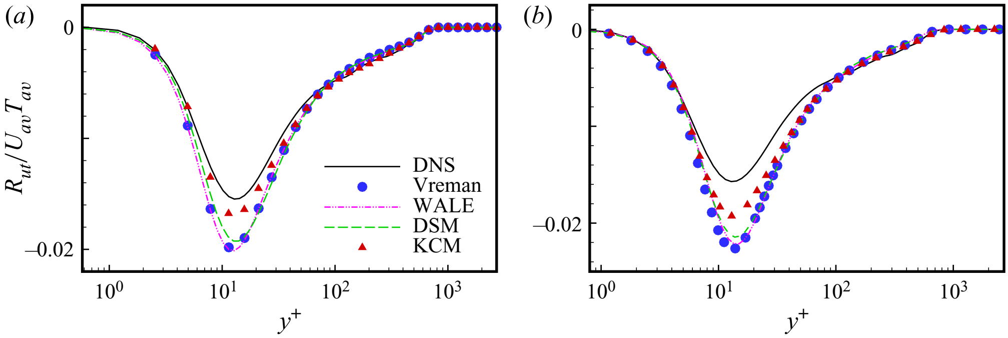

Figure 18. Temperature–velocity correlation normalized by the product of averaged temperature and velocity ($u_{av}T_{av}$) along the wall-normal direction at $x = 8.8$ of the compressible flat-plate boundary layer: (*a*) grid-1 and (*b*) grid-2.

Moreover, the distribution of the van Driest transformed mean streamwise velocity at $x = 8.8$ under the different scales of the grids are shown in

figure 17(*a*,*b*), where the flow can be regarded as steady turbulence. As seen from the two panels, both of the profiles predicted by KCM are always very close to the real values in all the regions. Conversely, the other models clearly overestimate the velocity in the buffer region, log-law region and defect-law region.

In figure 18(*a*,*b*), we display the normalized temperature–velocity correlation along the wall-normal direction at $x = 8.8$ for the two grid resolutions. In contrast to other models, the result from KCM in the case of the fine grid has the obvious advantage, but this is not so distinct in the coarse-grid case.

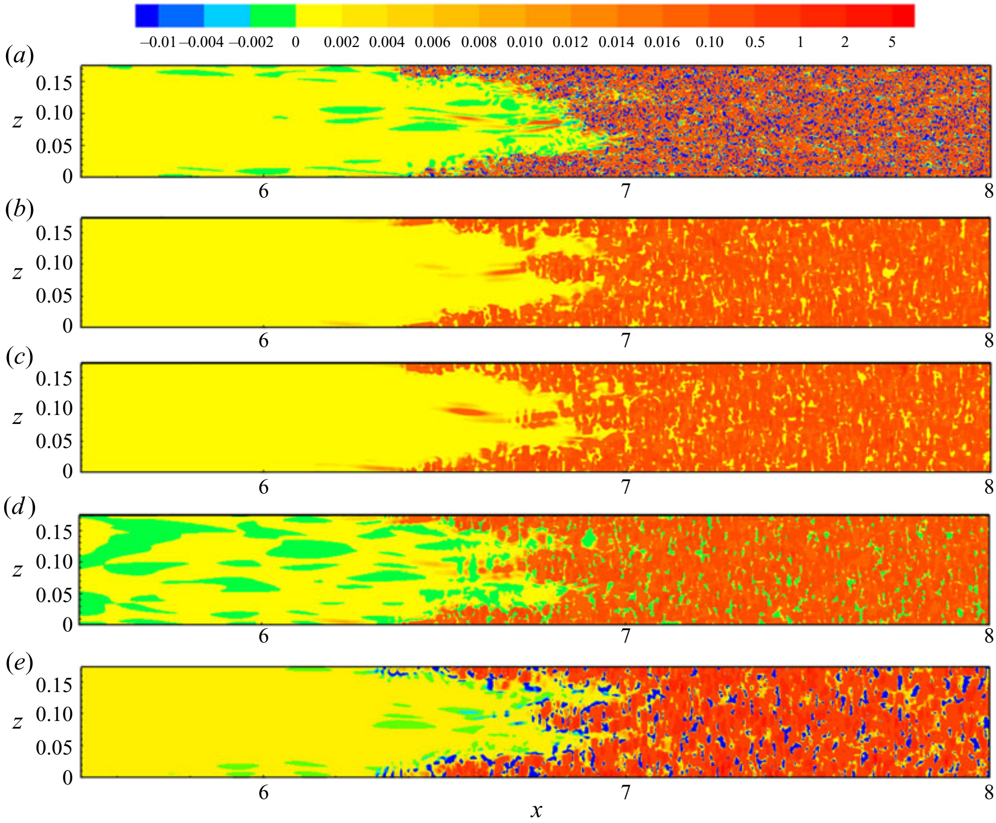

Figure 19. An *a posteriori* test of the local KEF of the compressible flat-plate boundary layer at $y^+ = 15$ from the LES models in the case of grid-1, and the real value for comparison: (*a*) the real value; (*b*) Vreman; (*c*) WALE; (*d*) DSM; and (*e*) KCM.

Figure 19 shows the *a posteriori* test of the local KEF obtained from the LES data of Vreman, WALE, DSM and KCM in the case of grid-1; the real KEF is also displayed here for comparison. From the figure, we find that the results are similar to those in the *a priori* test. The KEF from KCM and the real KEF have similar spatial distributions, and the backscatters are full of their flow fields. Even if the KEF obtained from DSM exist some weak local energy backscatters, the distribution of the local KEF is still greatly different from the real value. On the other hand, the KEF obtained from the traditional eddy-viscosity models still has no backscatter in the whole field, and the amplitudes of the forward cascades are higher than the real value, which indicates that the SGS models are more dissipative. Additionally, we can infer that KCM can predict KEF, energy backscatters and flow structures more accurately in this case.

Figure 20(*a*,*b*) shows the KEF ratio η_Δ of KCM along the streamwise direction at $y^+ = 15$ of the compressible flat-plate boundary layer in the two cases of different grid resolutions. The distribution trend of the KEF ratio is similar to that of the skin-friction coefficient in figure 16. Moreover, the value of η_Δ in the coarse-grid case is higher that in the fine-grid case, which also indicates that the proposed model will be much better than the model with the constraint from the original TD model on the coarse mesh. Figure 21 shows the model coefficients of the two cases with different grid resolutions. In the region

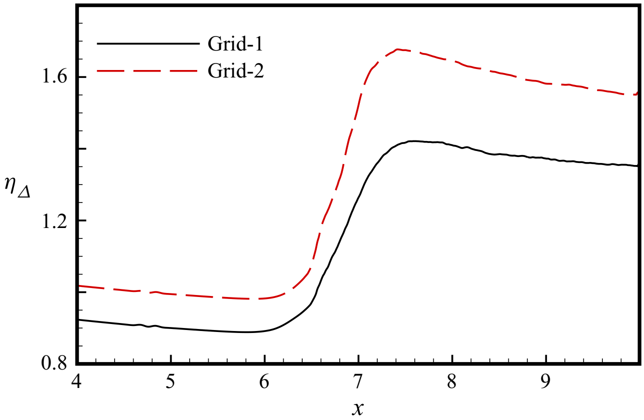

Figure 20. An *a posteriori* test of KEF ratio η_Δ of KCM along the streamwise direction at $y^+ = 15$ of the compressible flat-plate boundary layer at different grid resolutions: (*a*) grid-1 and (*b*) grid-2.

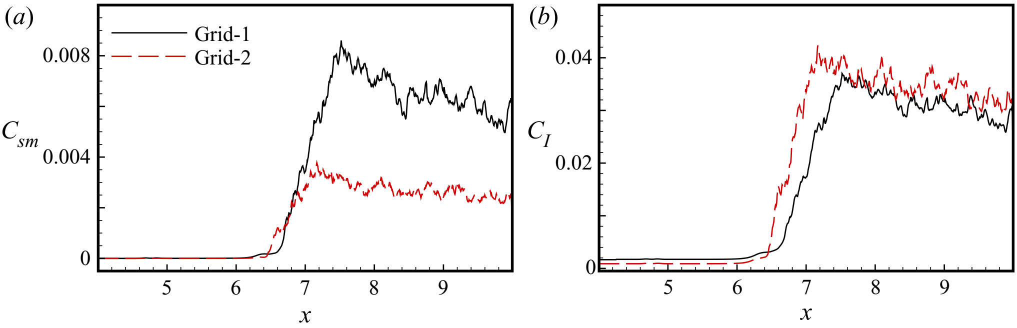

Figure 21. An *a posteriori* test of the model coefficients of KCM along the streamwise direction at $y^+ = 15$ of the compressible flat-plate boundary layer at different grid resolutions: (*a*) C_{sm} and (*b*) C_I.

$4 < x < 6.5$, all the model coefficients of the two cases are zero. It could also indicate that KCM is off in the laminar flow, and starts to work at the transition point. Also, the distributions of these model coefficients are similar to the distributions of the skin-friction coefficient.

6. Conclusions

In this paper, we propose a kinetic-energy-flux-constrained model (KCM) for the large-eddy simulation (LES) of compressible wall turbulent flows. The new proposed subgrid-scale (SGS) stress model aims to guarantee the proper prediction of the kinetic energy flux (KEF) and the robustness of the computation in LES of compressible wall-bounded turbulence. The KEF obtained from the tensor-diffusivity (TD) model has a high correlation with the real value, but the TD model has low numerical stability. In contrast, the KEF from the Smagorinsky model (SM) has a low correlation with the real value but has a high robustness in computation. At the same time, from theoretical analyses, we can confirm that the SM still has higher numerical stability than the TD model, even in the condition with the same SGS dissipation. Using the DNS data of compressible channel flow, through an artificial neural network (ANN), we obtain the

KEF ratio between the KEF from the TD model and the real value. Thus, the modelled KEF is obtained and then applied to constrain the SM. In addition, the ANN method is only applied to predict a dimensionless coefficient, which might be easy to generalize to the simulation of other turbulent flows.

The KCM is first applied to the simulation of compressible turbulent channel flow. Compared with other traditional eddy-viscosity SGS models, the KCM could more accurately predict typical statistical quantities, including the mean streamwise velocity, Reynolds stress, temperature–velocity correlation, etc. Furthermore, the new model can predict more abundant coherent turbulent structures in the channel flow. Then, the KCM is also tested in a supersonic spatially developing flat-plate flow. Through an *a priori* test, the feasibility of the KCM for LES of more complex wall-bounded turbulence is displayed. In an *a posteriori* test, the KCM could precisely predict the natural transition process, including the onset of transition and the transition peak. Moreover, the KCM could provide more accurate profiles of skin friction, the mean velocity profiles and temperature–velocity correlation in cases with two different grid resolutions. The new model could also predict the energy backscatters in transition and turbulent flows properly.

In summary, the new LES methodology suggested in this paper has been verified to be an effective method in LES. It can help to improve the prediction of both kinetic energy flux and SGS heat flux. Nevertheless, it should be mentioned that the new methodology still needs to be tested and modified in the wall-bounded turbulence with other types of complex-geometry boundaries.

Acknowledgements. The authors thank the National Supercomputer Center in Tianjin (NSCC-TJ) and the National Supercomputer Center in GuangZhou (NSCC-GZ) for providing computer time.

Funding. This work was supported by the National Key Research and Development Program of China (2020YFA0711800 and 2019YFA0405302) and NSFC Projects (Nos. 12072349, 91852203 and 91952104).

Declaration of interests. The authors report no conflict of interest.

Author ORCIDs.
Changping Yu https://orcid.org/0000-0002-2126-1344;
Zelong Yuan https://orcid.org/0000-0003-0279-111X;
Jianchun Wang https://orcid.org/0000-0001-5101-7791.

REFERENCES

Bardina, J., Ferziger, J. & Reynolds, W. 1980 Improved subgrid-scale models for large-eddy simulation. *AIAA Paper*, 80-1357.

Bodart, J. & Larsson, J. 2012 Sensor-based computation of transitional flows using wall-modelled large eddy simulation. *Center for Turbulence Research Annual Briefs 2012*, pp. 229–240.

Borue, V. & Orszag, S.A 1998 Local energy flux and subgrid-scale statistics in three-dimensional turbulence. *J. Fluid Mech.* **366**, 1–31.

Chai, X. & Mahesh, K. 2012 Dynamic-equation model for large-eddy simulation of compressible flows. *J. Fluid Mech.* **699**, 385–413.

Chaté, H. & Manneville, P. 1987 Transition to turbulence via spatio-temporal intermittency. *Phys. Rev. Lett.* **58** (2), 112.

Chen, S., Xia, Z., Pei, S., Wang, J., Yang, Y., Xiao, Z. & Shi, Y. 2012 Reynolds-stress-constrained large-eddy simulation of wall-bounded turbulent flows. *J. Fluid Mech.* **703**, 1–28.

Chollet, J.P. & Lesieur, M. 1981 Parameterization of small scales of three-dimensional isotropic turbulence utilizing spectral closures. *J. Atmos. Sci.* **38** (12), 2747–2757.

Clark, R.A., Ferziger, J.H. & Reynolds, W.C. 1979 Evaluation of subgrid-scale models using an accurately simulated turbulent flow. *J. Fluid Mech.* **91**, 1–16.

Coleman, G.N, Kim, J. & Moser, R.D. 1995 A numerical study of turbulent supersonic isothermal-wall channel flow. *J. Fluid Mech.* **305**, 159–183.

DEARDORFF, J.W. 1970 A numerical study of three-dimensional turbulent channel flow at large Reynolds numbers. *J. Fluid Mech.* **41**, 453–480.

DUCROS, F., COMTE, P. & LESIEUR, M. 1996 Large-eddy simulation of transition to turbulence in a boundary layer developing spatially over a flat plate. *J. Fluid Mech.* **326**, 1–36.

DURAISAMY, K., IACCARINO, G. & XIAO, H. 2019 Turbulence modeling in the age of data. *Annu. Rev. Fluid Mech.* **51**, 357–377.

EYINK, G.L. 2006 Multi-scale gradient expansion of the turbulent stress tensor. *J. Fluid Mech.* **549**, 159–190.

FOYSI, H., SARKAR, S. & FRIEDRICH, R. 2004 Compressibility effects and turbulence scalings in supersonic channel flow. *J. Fluid Mech.* **509**, 207–216.

FUKAMI, K., FUKAGATA, K. & TAIRA, K. 2019 Super-resolution reconstruction of turbulent flows with machine learning. *J. Fluid Mech.* **870**, 106–120.

FUREBY, C. 2008 Towards the use of large eddy simulation in engineering. *Prog. Aerosp. Sci.* **44**, 381–396.

GARNIER, E., ADAMS, N. & SAGAUT, P. 2000 *Large Eddy Simulation for Compressible Flows*. Springer.

GEORGIADIS, N.J., ALEXANDER, J.I. & RESHOTKO, E. 2001 Development of a hybrid rans/les method for compressible mixing layer. *AIAA Paper*, 2001-0289.

GERMANO, M., PIOMELLI, U., MOIN, P. & CABOT, W.H. 1991 A dynamic subgrid-scale eddy viscosity model. *Phys. Fluids* A **3** (7), 1760–1765.

GHOSAL, S., LUND, T.S., MOIN, P. & AKSELVOLL, K. 1995 A dynamic localization model for large-eddy simulation of turbulent flows. *J. Fluid Mech.* **286**, 229–255.

GHOSH, S., FOYSI, H. & FRIEDRICH, R. 2010 Compressible turbulent channel and pipe flow: similarities and differences. *J. Fluid Mech.* **648**, 155–181.

GÜEMES, A., DISCETTI, S., IANIRO, A., SIRMACEK, B., AZIZPOUR, H. & VINUESA, R. 2021 From coarse wall measurements to turbulent velocity fields through deep learning. *Phys. Fluids* **33**, 075121.

HORIUTI, K. 1986 On the use of sgs modelling in the simulation of transition in plane channel flow. *J. Phys. Soc. Japan* **55** (5), 1528–1541.

HUAI, X., JOSLIN, R.D. & PIOMELLI, U. 1997 Large-eddy simulation of transition to turbulence in boundary layers. *J. Theor. Comput. Fluid Dyn.* **9** (2), 149–163.

KIM, H., KIM, J., WON, S. & LEE, C. 2021 Unsupervised deep learning for super-resolution reconstruction of turbulence. *J. Fluid Mech.* **910**, A29.

KIM, J. & LEE, C. 2020 Prediction of turbulent heat transfer using convolutional neural networks. *J. Fluid Mech.* **882**, A18.

KINGERMA, D.P. & BA, J. 2019 Adam: a method for stochastic optimization. arXiv:1412.6980.

KOLMOGOROV, A.N. 1941 The local structure of turbulence in incompressible viscous fluid for very large Reynolds numbers. *C. R. Acad. Sci. URSS* **30**, 301–305.

LARCHEVÊQUE, L., SAGAUT, P., LÊ, T.H. & COMTE, P. 2004 Large-eddy simulation of a compressible flow in a three-dimensional open cavity at high Reynolds number. *J. Fluid Mech.* **516**, 265–301.

LEONI, P.C.D., ZAKI, T.A., KARNIADAKIS, G. & MENEVEAU, C. 2021 Two-point stress-strain-rate correlation structure and non-local eddy viscosity in turbulent flows. *J. Fluid Mech.* **914**, A6.

LESIEUR, M. & MÉTAIS, O. 1996 New trends in large-eddy simulations of turbulence. *Annu. Rev. Fluid Mech.* **28**, 45–82.

LI, W., FAN, Y., MODESTI, D. & CHENG, C. 2019 Decomposition of the mean skin-friction drag in compressible turbulent channel flows. *J. Fluid Mech.* **875**, 101–123.

LILLY, D.K. 1992 A proposed modification of the germano subgrid-scale closure method. *Phys. Fluids* A **238**, 633–635.

LING, J., KURZAWSKI, A. & TEMPLETON, J.P. 2016 Reynolds averaged turbulence modelling using deep neural networks with embedded invariance. *J. Fluid Mech.* **807**, 155–166.

LIU, S., MENEVEAU, C. & KATZ, J. 1994 On the properties of similarity subgrid-scale models as deduced from measurements in a turbulent jet. *J. Fluid Mech.* **275**, 83–119.

LIU, B., TANG, J., HUANG, H. & LU, X. 2020 Deep learning methods for super-resolution reconstruction of turbulent flows. *Phys. Fluids* **32**, 025105.

MARTIN, M.P.INO, PIOMELLI, U. & CANDLER, G.V 2000 Subgrid-scale models for compressible large-eddy simulations. *J. Theor. Comput. Fluid Dyn.* **13** (5), 361–376.

MAULIK, R. & SAN, O. 2017 A neural network approach for the blind deconvolution of turbulent flows. *J. Fluid Mech.* **831**, 151–181.

MENEVEAU, C. & KATZ, J. 2000 Scale-invariance and turbulence models for lage-eddy simulation. *Annu. Rev. Fluid Mech.* **32**, 1–32.

MENEVEAU, C. & LUND, T.S. 1997 The dynamic smagorinsky model and scale-dependent coefficients in the viscous range of turbulence. *Phys. Fluids* **9** (12), 3932–3934.

MENEVEAU, C., LUND, T.S. & CABOT, W.H. 1996 A lagrangian dynamic subgrid-scale model of turbulence. *J. Fluid Mech.* **319**, 353–385.

MENEVEAU, C & SREENIVASAN, K.R. 1987 Simple multifractal cascade model for fully developed turbulence. *Phys. Rev. Lett.* **59** (13), 1424.

MOIN, P., SQUIRES, K., CABOT, W. & LEE, S. 1991 A dynamic subgrid-scale model for compressible turbulence and scalar transport. *Phys. Fluids* A **3** (11), 2746–2757.

MORINISHI, Y., TAMANO, S. & NAKABAYASHI, K. 2004 Direct numerical simulation of compressible turbulent channel flow between adiabatic and isothermal walls. *J. Fluid Mech.* **512**, 273–308.

MOSER, R.D., HAERING, S.W. & YALLA, G.R. 2021 Statistical properties of subgrid-scale turbulence models. *Annu. Rev. Fluid Mech.* **53**, 255–286.

NICOUD, F. & DUCROS, F. 1999 Subgrid-scale stress modelling based on the square of the velocity gradient tensor. *Flow Turbul. Combust.* **63**, 183–200.

PARK, J. & CHOI, H. 2021 Toward neural-network-based large eddy simulation: application to turbulent channel flow. *J. Fluid Mech.* **914**, A16.

PECNIK, R. & PATEL, A. 2017 Scaling and modelling of turbulence in variable property channel flows. *J. Fluid Mech.* **823**, R1.

PICKERING, E., RIGAS, G., SCHMIDT, O.T., SIPP, D. & COLONIUS, T. 2021 Optimal eddy viscosity for resolvent-based models of coherent structures in turbulent jets. *J. Fluid Mech.* **917**, A29.

PIOMELLI, U. 1993 High reynolds number calculations using the dynamic subgrid-scale stress model. *Phys. Fluids* A **5** (6), 1484–1490.

PIOMELLI, U. 1999 Large-eddy simulation: achievements and challenges. *Prog. Aerosp. Sci.* **35** (4), 335–362.

PIROZZOLI, S., GRASSO, F. & GATSKI, T.B. 2004 Direct numerical simulation and analysis of a spatially evolving supersonic turbulent boundary layer at $M = 2.25$. *Phys. Fluids* **16**, 530–545.

POPE, S.B. 2000 *Turbulent Flows*. Cambridge University Press.

PORTÉ-AGEL, F., MENEVEAU, C. & PARLANGE, M. 2000 A scale-dependent dynamic model for large-eddy simulation: application to a neutral atmospheric boundary layer. *J. Fluid Mech.* **415**, 261–284.

SAYADI, T. & MOIN, P. 2012 large eddy simulation of controlled transition to turbulence. *Phys. Fluids* **24**, 114103.

SMAGORINSKY, J. 1963 General circulation experiments with the primitive equations: I. The basic experiment. *Mon. Weath. Rev.* **91**, 99–164.

TRITTON, D.J 2012 *Physical Fluid Dynamics*. Springer Science & Business Media.

VERSTAPPEN, R. 2004 A synthesis of similarity and eddy-viscosity models. In *Direct and Large-Eddy Simulation V*, pp. 271–278.

VINUESA, R. & BRUNTON, S.L. 2021 The potential of machine learning to enhance computational fluid dynamics. arXiv:2110.02085.

VOKE, P. 1996 Subgrid-scale modelling at low mesh Reynolds number. *Theor. Comput. Fluid Dyn.* **8**, 131–143.

VOLLANT, V., BALARAC, G. & CORRE, C. 2017 Subgrid-scale scalar flux modelling based on optimal estimation theory and machine-learning procedures. *J. Turbul.* **18** (9), 854–878.

VREMAN, A.W. 2004 An eddy-viscosity subgrid-scale model for turbulent shear flow: algebraic theory and applications. *Phys. Fluids* **16**, 3670–3681.

VREMAN, A.W., GEURTS, B.J. & DEEN, N.G. 2004 Large-eddy simulation of particle-laden turbulent channel flow. In *Direct and Large-Eddy Simulation V*, pp. 271–278.

VREMAN, B., GEURTS, B.J., DEEN, N.G., KUIPERS, J.A.M. & KUERTEN, J.G.M. 2009 Two- and four-way coupled euler-lagrangian large-eddy simulation of particle-laden turbulent channel flow. *Flow Turbul. Combust.* **82**, 47–71.

VREMAN, A.W., GEURTS, B. & KUERTEN, H. 1995 Subgrid-modelling in les of compressible flow. *Appl. Sci. Res.* **54**, 181–203.

VREMAN, B., GEURTS, B. & KUERTEN, H. 1996 Large-eddy simulation of the temporal mixing layer using the clark model. *J. Theor. Comput. Fluid Dyn.* **8** (4), 309–324.

WANG, J., YANG, Y., SHI, Y., XIAO, Z., HE, X.T. & CHEN, S. 2013 Cascade of kinetic energy in three-dimensional compressible turbulence. *Phys. Rev. Lett.* **110** (21), 214505.

XIE, C., WANG, J., LI, H., WAN, M. & CHEN, S. 2019 Artificial neural network mixed model for large eddy simulation of compressible isotropic turbulence. *Phys. Fluids* **31**, 085112.

XIE, C., WANG, J. & WEINAN, E. 2020*a* Modeling subgrid-scale forces by spatial artificial neural networks in large eddy simulation of turbulence. *Phys. Rev. Fluids* **5**, 054606.

XIE, C., YUAN, Z. & WANG, J. 2020*b* Artificial neural network-based nonlinear algebraic models for large eddy simulation of turbulence. *Phys. Fluids* **32**, 115101.

YANG, X.I.A. & LV, Y. 2018 A semi-locally scaled eddy viscosity formulation for LES wall models and flows at high speeds. *J. Theor. Comput. Fluid Dyn.* **32** (5), 617–627.

YANG, X.I.A., ZAFAR, S., WANG, J.X. & XIAO, H. 2019 Predictive large-eddy-simulation wall modeling via physics-informed neural networks. *Phys. Rev. Fluids* **4**, 034602.

YOSHIZAWA, A. 1986 Statistical theory for compressible turbulent shear flows, with the application to subgrid modeling. *Phys. Fluids* **29**, 2255–2271.

YU, C., HONG, R., XIAO, Z. & CHEN, S. 2013 Subgrid-scale eddy viscosity model for helical turbulence. *Phys. Fluids* **25**, 095101.

YU, C., XIAO, Z. & LI, X. 2016 Dynamic optimization methodology based on subgrid-scale dissipation for large eddy simulation. *Phys. Fluids* **28** (1), 015113.

YUAN, Z., XIE, C. & WANG, J. 2020 Deconvolutional artificial neural network models for large eddy simulation of turbulence. *Phys. Fluids* **32**, 115106.

ZHANG, P., WAN, Z. & SUN, D. 2019 Space-time correlations of velocity in a mach 0.9 turbulent round jet. *Phys. Fluids* **31**, 115108.

ZHOU, Z., HE, G., WANG, S. & JIN, G. 2019*b* Subgrid-scale model for large-eddy simulation of isotropic turbulent flows using an artificial neural network. *Comput. Fluids* **195**, 104319.

ZHOU, H., LI, X., QI, H. & YU, C. 2019*a* Subgrid-scale model for large-eddy simulation of transition and turbulence in compressible flows. *Phys. Fluids* **31**, 125118.